


## Anatomy of Type- $x$ Spin-Orbit-Torque Switching

Yan-Ting Liu<sup>1,†</sup>, Chao-Chung Huang<sup>1,†</sup>, Kuan-Hao Chen<sup>1</sup>, Yu-Hao Huang<sup>1</sup>, Chia-Chin Tsai<sup>1</sup>, Ting-Yu Chang<sup>1</sup>, and Chi-Feng Pai<sup>1,2,\*</sup>

<sup>1</sup>*Department of Materials Science and Engineering, National Taiwan University, Taipei 10617, Taiwan*

<sup>2</sup>*Center of Atomic Initiative for New Materials, National Taiwan University, Taipei 10617, Taiwan*

 (Received 12 May 2021; revised 23 June 2021; accepted 27 July 2021; published 12 August 2021)

Using a type- $x$  spin-orbit-torque (SOT) switching scheme, in which the easy axis (EA) of the ferromagnetic (FM) layer and the charge-current flow direction are collinear, it is possible to realize a lower-power-consumption, higher-density, and better-performance SOT magnetoresistive random-access memory (SOT MRAM) compared with the conventional type- $y$  design. Here, we systematically investigate type- $x$  SOT switching properties through both macrospin and micromagnetic simulations. The out-of-plane external field and anisotropic field dependence of the switching-current density ( $J_{sw}$ ) is first examined in the ideal type- $x$  configuration. Next, we study the FM-layer canting-angle ( $\varphi$ ) dependence of  $J_{sw}$  through macrospin simulations and experiments, which show the transformation of switching dynamics from type  $x$  to type  $y$  with increasing  $\varphi$ . By further integrating fieldlike torque (FLT) into the simulated system, we find that a positive FLT can assist type- $x$  SOT switching, while a negative one brings about complex dynamics. More crucially, with the existence of a sizable FLT, type- $x$  switching mode results in a lower critical switching current than that of type  $y$  at a current pulse width less than about 10 ns, indicating the advantage of employing the type- $x$  design for ultrafast switching using material systems with FLT. Our work provides a thorough examination of the type- $x$  SOT scheme with various device and materials parameters, which can be informative for designing next-generation SOT MRAM.

DOI: [10.1103/PhysRevApplied.16.024021](https://doi.org/10.1103/PhysRevApplied.16.024021)

### I. INTRODUCTION

The current-induced bulk spin Hall effect [1,2] (SHE) from heavy metals (HMs) and the interfacial Rashba-Edelstein effect [3] (REE) are capable of exerting spin-orbit torques (SOTs) upon an adjacent ferromagnetic (FM) layer, providing a promising approach to manipulate magnetization to achieve high-frequency oscillation [4–6], domain-wall motion [7–9], and SOT-induced magnetization switching [3,10–14]. Spin-torque-driven [such as spin-transfer torque (STT) and SOT] magnetization switching is promising technology for magnetic random-access memory (MRAM) applications. Unlike the vulnerability of conventional STT MRAM based on the STT mechanism [15], SOT MRAM has the advantage of low power consumption, faster switching, and separation of read and write paths, to guarantee high endurance, approaching industrial needs. There are three different types of SOT-switching schemes, i.e., type  $x$ , type  $y$ , and type  $z$  [16–18]. Type- $z$  geometry has a FM pillar with perpendicular magnetic anisotropy (PMA). For type- $x$  (type- $y$ ) geometry, the magnetic easy axis of the FM pillar lies

in the FM-film plane and is collinear with (orthogonal to) the applied current. It has been shown that type  $y$  requires a current with a longer pulse width to achieve deterministic switching, which limits the performance of the type- $y$  device in the short-pulse regime [18,19]. In contrast, for type- $x$  and type- $z$  geometries, where the orthogonal spin polarization ( $\hat{\sigma}$ ) dominates, SOT-induced magnetization switching takes place with little precession, making them less sensitive to the applied-current pulse width. At the short-current-pulse regime, compared with type- $y$  geometry, a smaller switching-current density ( $J_{sw}$ ) of type  $x$  and type  $z$  has been demonstrated via numerical simulation [16] and experiment [19]. However, due to the noncollinearity between  $\hat{\sigma}$  and magnetization in type- $z$  and type- $x$  configurations, an external field is required to break symmetry and achieve deterministic switching [20]. For type  $z$ , field-free deterministic switching can be realized by introducing a voltage-controlled electric field [21], the assistance of an exchange-bias field from the antiferromagnetic layer [22], a wedge structure [12,23], an additional FM layer with in-plane anisotropy [24–26], geometrical domain-wall pinning [27], competing spins from materials with opposite spin Hall angles [28,29], or lateral SOT from localized laser annealing [30]. These approaches are typically challenging to achieve in nanosized devices. For

\*cfpai@ntu.edu.tw

†These authors contributed equally to this work.

TABLE I. Switching characteristics of type- $z$ , type- $y$ , and type- $x$  geometries. PMA (IMA) represents perpendicular (in-plane) magnetic anisotropy.

	Type $z$	Type $y$	Type $x$
Magnetic anisotropy	PMA	IMA	IMA
Easy-axis (EA) direction	EA $\perp$ $x$ - $y$ plane EA $\perp$ $\hat{\sigma}$	EA $\parallel$ $y$ EA $\parallel$ $\hat{\sigma}$	EA $\parallel$ $x$ EA $\perp$ $\hat{\sigma}$
Achieve field-free switching?	No, $\mu_0 H_x$ is required	Yes	No, $\mu_0 H_z$ is required
Methods to achieve field-free switching	1. Additional voltage-controlled electric field [21] 2. Exchange-bias field [22] 3. Wedge structure [12,23] 4. Additional FM layer with IMA [24–26] 5. Geometrical domain-wall pinning [27] 6. Competing spins [28,29] 7. Localized laser annealing [30]	No need	1. Canted EA in FM layer [16,19,31] 2. Additional FM layer with PMA [16]

type  $x$ , there is a much simpler way to achieve field-free switching through structural engineering: introducing a small tilting angle between the easy axis of the FM pillar and the current channel [16,19,31]. A brief summary of the characteristics of these three SOT switching schemes can be found in Table I.

Here, we systemically investigate type- $x$  SOT switching properties in a nanosized HM/FM bilayer structure by macrospin and micromagnetic simulations. First, we demonstrate that  $J_{\text{sw}}$  in the type- $x$  SOT switching scheme can be modified by external field  $\mu_0 H_z$ , a uniaxial-anisotropy field, and a shape-anisotropy field. Next, field-free switching for type- $x$  geometry is verified by canting the major axis orientation of the FM pillar. Through canting-angle-dependence simulations, we observe a sharp transition from type- $x$  to type- $y$  switching behavior as the canting angle increases. We also experimentally verify this switching dynamic change by measuring  $J_{\text{sw}}$  versus canting angle  $\varphi$  in representative HM/FM bilayer devices (HM, W; FM, Co-Fe-B). From a pulse-width-dependence simulation using type- $x$  and type- $y$  geometries, we show that the switching current ( $I_{\text{sw}}$ ) of type  $x$  is indeed smaller than that of type  $y$ , but only in the *extremely short* pulse-width ( $<0.2$  ns) regime. A detailed switching phase diagram with various fieldlike torque (FLT) to dampinglike torque (DLT) ratios and applied current densities ( $J_{\text{applied}}$ ) is obtained to gain an insight into all possible magnetization dynamics. For a FLT-to-DLT ratio of  $>0$ , only deterministic switching and nonswitching can be obtained.  $J_{\text{sw}}$  reduces significantly with increasing FLT. On the other hand, for a FLT-to-DLT ratio of  $<0$ , more complex magnetization dynamics can emerge. Lastly, through both macrospin and micromagnetic simulations, we show that  $I_{\text{sw}}$  of the field-free type- $x$  scheme can be reduced by increasing the FLT-to-DLT ratio. The crossover of  $I_{\text{sw}}$  versus  $t_{\text{pulse}}$  curves for type  $x$  and type  $y$  gradually moves to a longer pulse regime ( $>1$  ns) with increasing

FLT-to-DLT ratio, which points out the benefit of employing magnetic heterostructures with a sizable FLT for type- $x$  SOT applications.

## II. RESULTS AND DISCUSSION

The magnetization dynamics in the FM layer is described by the Landau-Lifshitz-Gilbert equation with an additional dampinglike SOT (DLT) term:

$$\frac{d\mathbf{m}}{dt} = -\gamma \mathbf{m} \times \mathbf{H}_{\text{eff}} + \alpha \mathbf{m} \times \frac{d\mathbf{m}}{dt} + \gamma \frac{\hbar \xi_{\text{DL}} J_{\text{applied}}}{2eM_s t_{\text{FM}}} \mathbf{m} \times (\hat{\sigma} \times \mathbf{m}), \quad (1)$$

where  $\gamma$  is the gyromagnetic ratio,  $\alpha$  is the Gilbert damping constant,  $M_s$  is the saturation magnetization of the FM pillar,  $J_{\text{applied}}$  is the applied current density,  $t_{\text{FM}}$  is the thickness of the FM layer,  $\hat{\sigma}$  is the orientation of spin polarization accumulated at the HM/FM interface, and  $\xi_{\text{DL}}$  is the DLT efficiency. The effective field,  $\mathbf{H}_{\text{eff}} = \mathbf{H}_{\text{ext}} + \mathbf{H}_K + \mathbf{H}_d$ , is composed of the external field, uniaxial-anisotropy field, and shape-anisotropy field. To get closer to realistic scenarios, we use the parameters listed in Table II. The size of the FM nanopillar is  $60 \times 30 \times 1 \text{ nm}^3$  ( $L \times W \times t_{\text{FM}}$ ). Since the experimentally determined magnitude of  $\xi_{\text{DL}}$  for tungsten (W) is about 0.3 to 0.5 [11,32–35], we tentatively set  $|\xi_{\text{DL}}| = 0.5$  for the HM layer in our simulation. The width of the HM layer is equal to the width of the FM pillar along  $y$ . The thickness of the HM layer ( $t_{\text{HM}}$ ) is 3 nm, which is longer than the spin-diffusion length of W [13,36].

### A. Three schemes of SOT switching

Schematics of the type- $x$ ,  $-y$ , and  $-z$  switching configurations are shown in Figs. 1(a)–1(c). For type- $x$  (type- $y$ ) geometry, the easy axis of the FM pillar is collinear with (orthogonal to) the current-channel direction. Notably, the

TABLE II. Detailed parameters adopted in macrospin and micromagnetic simulations.

	Symbol (unit)	Macrospin simulation	Micromagnetic simulation
Saturation magnetization	$M_s$ (emu/cc)	1100	1100
Damping constant	$\alpha$	0.02 (for IMA) 0.1 (for PMA)	0.02
Uniaxial-anisotropy energy density	$K_u$ (J/m <sup>3</sup> )	$-8 \times 10^5$ (for IMA) $+8 \times 10^5$ (for PMA)	0
FM pillar size	$V_{\text{pillar}}$ (nm <sup>3</sup> )	$60 \times 30 \times 1$ (for IMA) $30 \times 30 \times 1$ (for PMA)	$60 \times 30 \times 1$
Thickness (HM layer)	$t_{\text{HM}}$ (nm)	3	3
DLT efficiency	$ \xi_{\text{DL}} $	0.5	0.5
Interfacial DMI energy density	$D$ (J/m <sup>2</sup> )	—	$2 \times 10^{-4}$
Exchange-stiffness constant	$A$ (J/m)	—	$1.6 \times 10^{-11}$
Cell size	$V_{\text{cell}}$ (nm <sup>3</sup> )	—	$3 \times 3 \times 1$

easy axis of the FM pillar is mainly induced by shape anisotropy for in-plane magnetized systems. For type-z geometry, the easy axis is perpendicular to the FM pillar

plane ( $x$ - $y$  plane). The current is applied along the  $\pm x$  direction and  $\hat{\sigma}$  at the HM/FM interface thus points in the  $\pm y$  direction. To break symmetry, we set the external

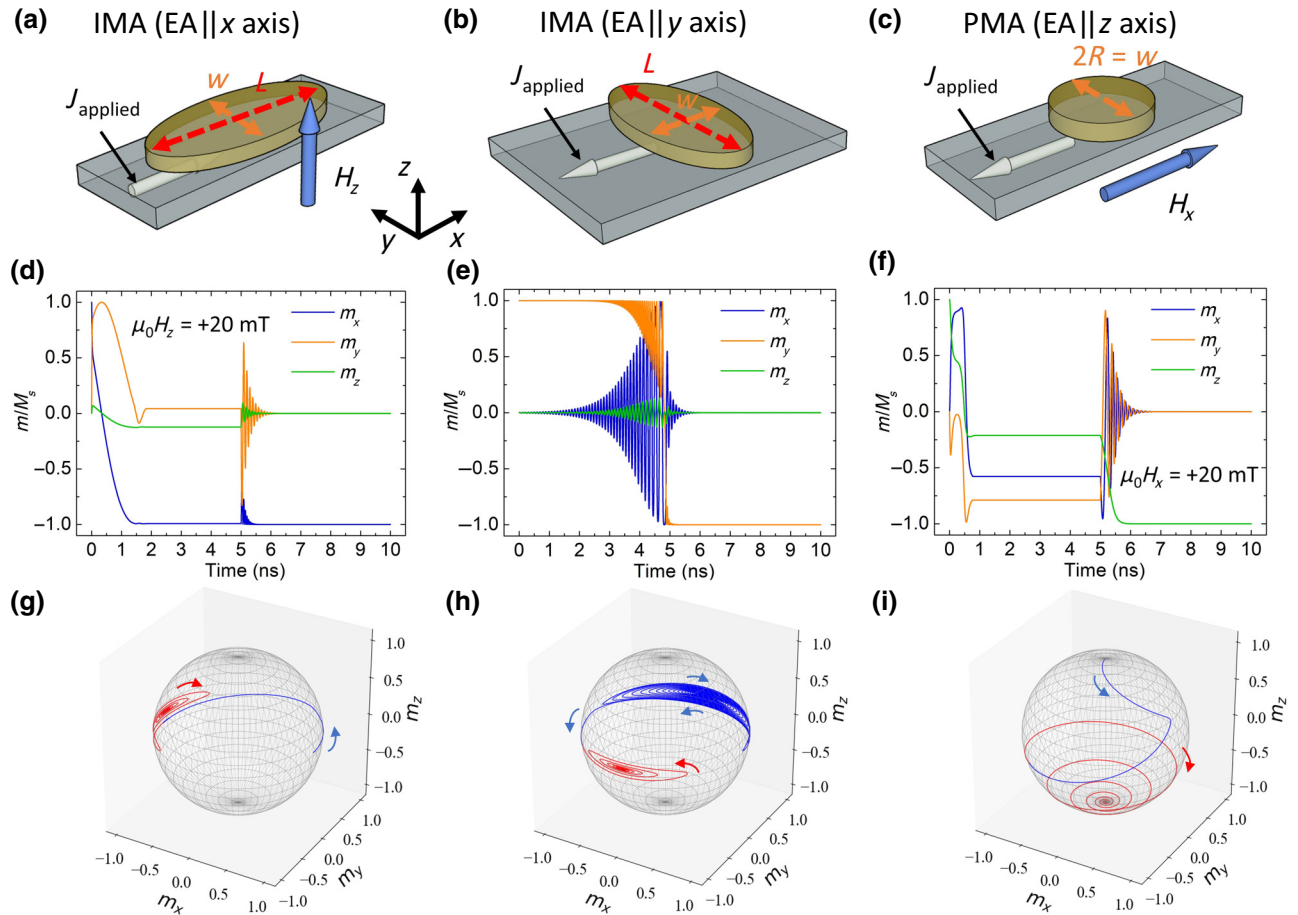


FIG. 1. Macrospin simulations. Schematic illustrations of (a) type-x, (b) type-y, and (c) type-z SOT switching. IMA and PMA represent FM pillars with in-plane magnetic anisotropy and out-of-plane magnetic anisotropy, respectively. Magnetization dynamics of (d) type-x, (e) type-y, and (f) type-z schemes under the excitation of SOT for 5 ns. 3D magnetization trajectories of (g) type-x, (h) type-y, and (i) type-z switching. External field (20 mT) along  $+z$  direction and  $+x$  direction is required to achieve deterministic switching for type-x and type-z structures, respectively. In (d)–(f),  $x$ ,  $y$ , and  $z$  components of magnetization,  $m_x$ ,  $m_y$ , and  $m_z$ , are denoted by blue, orange, and green lines, respectively. In (g)–(i), trajectories are divided into excitation segments (blue lines) and relaxation segments (red lines).

field to  $\mu_0 H_x = +20$  mT and  $\mu_0 H_z = +20$  mT for type- $z$  and type- $x$  configurations, respectively. Figures 1(d)–1(f) show the time evolution of magnetization for these three schemes with 5-ns duration of the applied current (and external field) and 5-ns relaxation. We also show the three-dimensional (3D) plot of magnetization trajectories with  $(m_x, m_y, m_z)$  coordinates in Figs. 1(g)–1(i).

For type- $y$  geometry, where collinear spin polarization dominates, the switching dynamics are quite different from those of type- $x$  and type- $z$ . The type- $y$  system goes through more precessions during the SOT-driven magnetization-switching process. For systems where orthogonal spin polarization dominates, the magnetization of type- $x$  (type- $z$ ) is almost directly switched from  $+x$  ( $+z$ ) to the  $-x$  ( $-z$ ) region without precession when the current pulse is turned on. Since the magnetization for type- $x$  geometry is affected by two different shape-anisotropy fields ( $\mathbf{H}_{d,y}$  and  $\mathbf{H}_{d,z} + H_K$ ) along the  $y$  and  $z$  directions, while type- $z$  geometry is only influenced by uniaxial anisotropy, the two switching modes are similar but with a slight variation.

### B. $\mu_0 H_z$ dependence of type- $x$ SOT switching

We first examine the  $\mu_0 H_z$  dependence of  $J_{sw}$  in the type- $x$  case. The representative device geometry is set as  $60 \times 30 \times 1$  nm<sup>3</sup> and  $K_u$  is set to be  $-8 \times 10^5$  J/m<sup>3</sup> with a uniaxial-anisotropy unit vector  $u = [0, 0, 1]$ . An external field  $\mu_0 H_z$  for the type- $x$  structure is required to achieve deterministic switching.  $J_{sw}$  is defined as the threshold current-density value at which magnetization can be deterministically switched. Initial position of magnetization is defined as  $m_x \sim +1$ . As shown in Fig. 2(a),  $J_{sw}$  decreases linearly to  $\mu_0 H_z$ . Since  $\hat{\sigma}$  is perpendicular to the easy-axis

direction in both type- $z$  and type- $x$  schemes, the switching dynamics of type- $x$  should be similar to that of type- $z$ . We then fit data with the equation derived analytically by Lee *et al.* [37] (modified for type- $x$ ):

$$\frac{dJ_{sw}}{d\mu_0 H_z} = -\frac{2e}{\sqrt{2}\hbar} \frac{M_s t_{FM}}{\xi_{DL}}, \quad (2)$$

where  $dJ_{sw}/d\mu_0 H_z$  is the extracted slope from the  $J_{sw}$  versus  $\mu_0 H_z$  curve. From linear fitting, we can obtain the slope,  $dJ_{sw}/d\mu_0 H_z = -5.73 \times 10^{12}$  A/Tm<sup>2</sup>, and the  $x$  intercept,  $\mu_0 H_{z,0} = 0.40$  T. The magnitude of the slope ( $dJ_{sw}/d\mu_0 H_z$ ) is comparable to the number extracted for the type- $z$  system [37]. More importantly, seminal work by Fukami *et al.* on type- $x$  switching also demonstrated that the linear trend between switching-current density and  $\mu_0 H_z$  can be observed via both experiments and simulations [16]. Therefore, we find that the external-bias-field dependences of SOT-driven switching-current densities for type- $x$  (using  $\mu_0 H_z$ ) and type- $z$  schemes (using  $\mu_0 H_x$ ) are quite similar.

### C. Uniaxial- and shape-anisotropy dependence of type- $x$ switching

Since  $J_{sw}$  also depends on the interfacial, bulk, and shape anisotropy of the device [16], we examine the influence of uniaxial-anisotropy energy density ( $K_u$ ) and the shape effect (aspect ratio) of the FM pillar on  $J_{sw}$  for the type- $x$  geometry. As shown in Fig. 2(b), when  $K_u$  varies from 0 to  $-1 \times 10^6$  J/m<sup>3</sup> with  $u = [0, 0, 1]$ , both the effective out-of-plane anisotropy field,  $\mu_0 H_{k,out}$ , and  $J_{sw}$  ( $\mu_0 H_z = +20$  mT) increase with respect to the magnitude

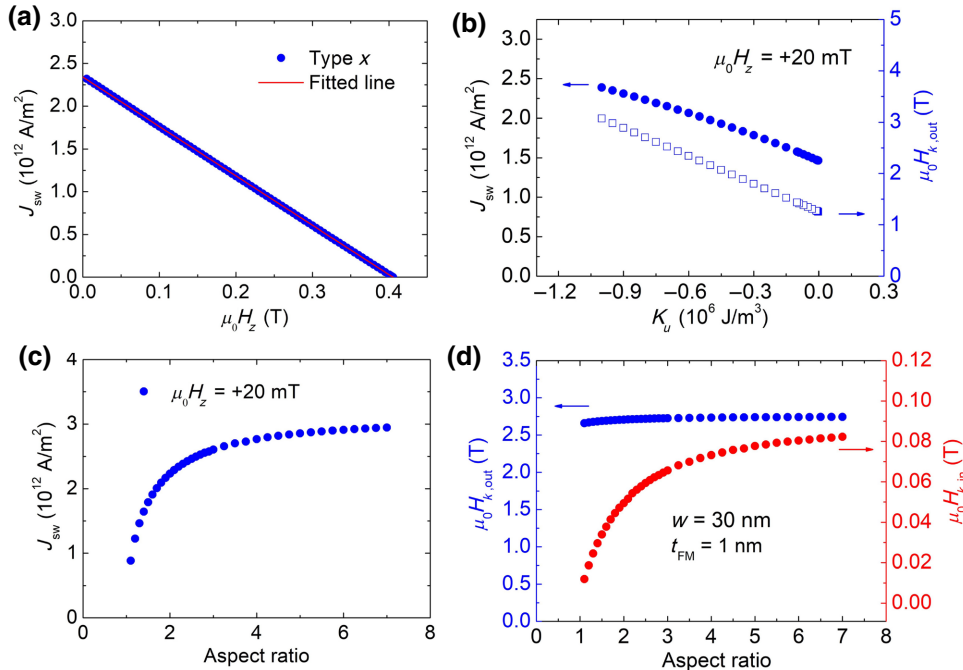


FIG. 2. Macrospin simulations. Critical switching-current density,  $J_{sw}$ , for type- $x$  geometry as a function of (a)  $z$ -direction external field  $\mu_0 H_z$  and (b) magnetic anisotropy energy density,  $K_u$ . Representative device geometry is set as  $60 \times 30 \times 1$  nm<sup>3</sup>;  $K_u$  is  $-8 \times 10^5$  J/m<sup>3</sup> with a uniaxial-anisotropy unit vector  $u = [0, 0, 1]$ . Open squares in (b) represent the magnitude of  $\mu_0 H_{k,out}$ . Filled circles in (b) represent the magnitudes of  $J_{sw}$ . (c)  $J_{sw}$ , (d)  $\mu_0 H_{k,out}$ , and  $\mu_0 H_{k,in}$  for type- $x$  structures as functions of the FM pillar's aspect ratio.

of  $K_u$ . Notably,  $K_u = 0$  means that only shape anisotropy is considered. We set  $K_u$  as  $-8 \times 10^5$  J/m<sup>3</sup> for further simulations.

To investigate the importance of shape engineering, we calculate  $J_{sw}$  as a function of the pillar aspect ratio, minor-axis length, and thickness of the FM layer. The shape-anisotropy field is estimated by  $-N_d M_S$ , where  $N_d$  is the demagnetization factor and is calculated from the major-axis length, minor-axis length, and thickness of the FM pillar [38]. In the aspect-ratio-dependence simulations, the minor-axis length and thickness of the FM pillar are fixed at 30 and 1 nm, respectively. We modify the length of the pillar's major axis from 30 to 218 nm (aspect ratio = 1.00 to 7.25). As shown in Fig. 2(c),  $J_{sw}$  becomes larger with increasing aspect ratio of the FM pillar and saturates at an aspect ratio of about 7.0. Out-of-plane and in-plane effective anisotropy fields,  $\mu_0 H_{k,out}$  and  $\mu_0 H_{k,in}$ , are also shown in Fig. 2(d) with various aspect ratios.  $\mu_0 H_{k,out}$  only slightly increases with increasing aspect ratio, while  $\mu_0 H_{k,in}$  is enhanced significantly with an increase in aspect ratio, which suggests that the aspect ratio affects  $\mu_0 H_{k,in}$  and then  $J_{sw}$ .  $J_{sw}$  versus minor-axis length and  $J_{sw}$  versus FM layer thickness also mainly depend on  $\mu_0 H_{k,in}$  versus minor-axis length or FM thickness (details of the minor-axis length and FM pillar-thickness dependence can be found in Supplemental Material S1 [39]).

According to the results of shape-dependent simulations, we conclude that  $J_{sw}$  strongly depends on  $\mu_0 H_{k,in}$ , which can be modified by the shape of the FM pillar. More specifically, a lower  $J_{sw}$  can be achieved by reducing  $\mu_0 H_{k,in}$  through shape engineering by choosing a smaller aspect ratio. However, since the thermal stability of the

device is proportional to the volume of the FM pillar and  $\mu_0 H_{k,in}$  (thereby its aspect ratio), an optimized aspect ratio should be chosen in realistic memory applications to lower the switching current, while maintaining reasonable thermal stability. For simplicity and generality, we choose the major-axis length, minor-axis length, and thickness of the FM pillar to be 60, 30, and 1 nm, respectively, for the following simulation tests.

#### D. Pulse-width dependence of type-x and type-y switching

To compare the performance between type-x and type-y structures in the short pulse-width regime, we calculate  $J_{sw}$  with various pulse widths ( $0.1 \text{ ns} \leq t_{pulse} \leq 10 \text{ ns}$ ) followed by 5-ns relaxation. It is noted that the pillar of the type-x system is canted toward the  $-y$  direction by about  $1^\circ$  to break symmetry; thus, no  $\mu_0 H_z$  is required [16,19,31]. The geometries of the simulated devices, type x ( $\varphi = 1^\circ$ ) and type y ( $\varphi = 90^\circ$ ), are shown in Fig. 3(a). The current-channel width is set to be the same as the pillar size along the  $y$  direction, i.e., 30 nm for type x and 60 nm for type y. It can be seen that one of the advantages of employing the type-x structure is the possibility of using a much narrower current channel. Based on these assumptions, we calculate the critical switching current,  $I_{sw}$ , for both type-x and type-y structures with various pulse widths, as shown in Fig. 3(b). The results indicate that  $I_{sw}$  versus  $t_{pulse}$  of type x changes more gradually than type y. The two sets of data cross over at  $t_{pulse} \sim 0.23 \text{ ns}$ , which is denoted as  $t_{CO}$ . This suggests that only in the extremely short pulse regime (sub-ns), type x outperforms type-y switching.

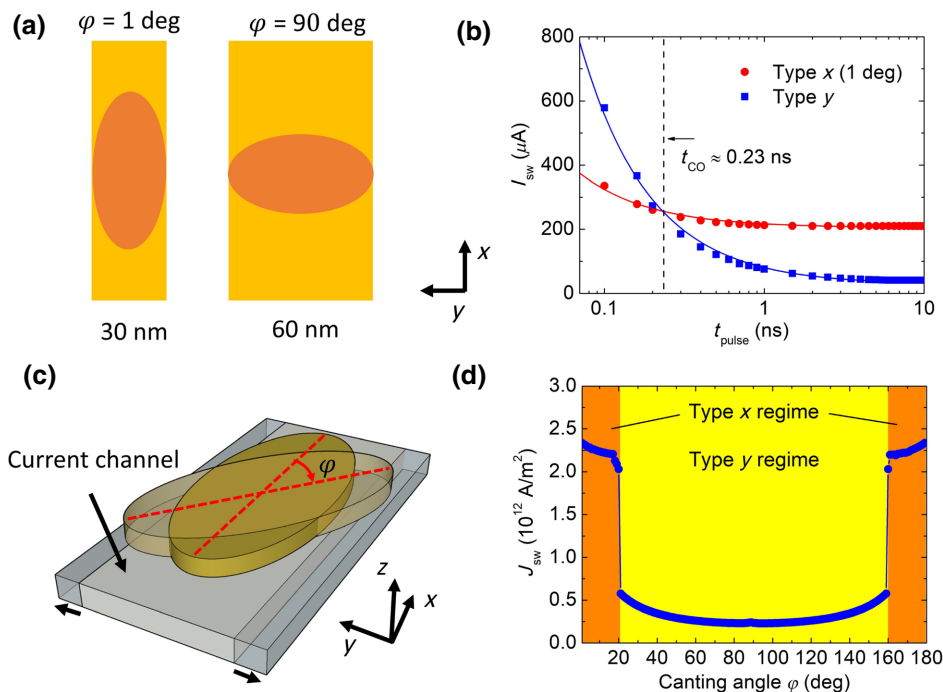


FIG. 3. Macrospin simulations. (a) Schematics of the simulated device with pillar canting angles of  $\varphi = 1^\circ$  (type x) and  $\varphi = 90^\circ$  (type y). (b) Current-pulse-width, dependence of switching current,  $I_{sw}$ , for type-x ( $\varphi = 1^\circ$ ) and type-y ( $\varphi = 90^\circ$ ) structures. Red and blue lines are fitted by Eq. (3). Dashed line represents the crossover point,  $t_{CO}$ , between the type-x and type-y geometry. (c) Schematics of the simulated device being canted away from the x direction. (d)  $J_{sw}$  calculated by varying  $\varphi$  under zero external magnetic field.

For fast precessional switching in the nanosecond or sub-nanosecond regimes, the pulse-width dependence of  $I_{\text{sw}}$  can be further fitted by [15,40–42]

$$I_{\text{sw}} = I_{\text{sw},0} \left( 1 + \frac{\tau_0}{t_{\text{pulse}}} \right), \quad (3)$$

where  $I_{\text{sw},0}$  is the intrinsic critical switching current and  $\tau_0$  is the precession time. From Eq. (3), we extract  $\tau_0 \approx 0.06$  ns for type- $x$  geometry and  $\tau_0 \approx 1.11$  ns for type  $y$ . Therefore, type  $x$  indeed has potential in high-speed SOT switching applications but only in the sub-nanosecond regime.

### E. Canting-angle dependence of SOT switching

Previous studies have demonstrated that type- $x$  devices can achieve field-free SOT switching by tilting the orientation of the FM pillar major axis towards the  $y$  direction to break symmetry [16,19,31]. In this section, we further simulate the pillar canting-angle dependence of  $J_{\text{sw}}$ . The schematics of the FM pillar for type  $x$  being canted from the current-channel direction by  $\varphi = 1^\circ$  to  $179^\circ$  are shown in Fig. 3(c). Notably, no external fields are included in the simulations in this section. As shown in Fig. 3(d), field-free switching can be achieved with  $J_{\text{sw}} = 2.3 \times 10^{12}$  A/m<sup>2</sup> for the type- $x$  geometry at  $\varphi = 1^\circ$ . The trend of  $J_{\text{sw}}$  versus  $\varphi$  is almost symmetric about  $90^\circ$ , as expected. When the canting angle  $\varphi$  increases from  $1^\circ$  to  $90^\circ$ , the switching-current density decreases rapidly at  $\varphi \sim 21^\circ$ , which indicates that the magnetization dynamics transform from type- $x$  to type- $y$  behavior at this particular canting angle. We can therefore divide the angle dependence into two zones: those

with higher  $J_{\text{sw}}$  ( $\varphi = 1^\circ$  to  $21^\circ$  and  $159^\circ$  to  $179^\circ$ ) belong to the “type- $x$  regime” [orange region in Fig. 3(d)], while the other part ( $\varphi = 22^\circ$  to  $158^\circ$ ) with a much smaller  $J_{\text{sw}}$  is the “type- $y$  regime” [yellow region in Fig. 3(d)].

To verify the canting-angle effect from macrospin simulations, we prepare a series of W(3)/Co-Fe-B(2.5)/MgO(1) (numbers in parentheses are in nanometers) Hall-bar devices with lateral dimensions of  $5 \times 60 \mu\text{m}^2$ , as schematically shown in Fig. 4(a). Details of thin-film and device preparation can be found in a previous study [14]. These devices are further annealed at  $220^\circ\text{C}$  for 20 min by applying an in-plane magnetic field of 0.25 T along a specific direction with respect to the Hall-bar device to establish an easy axis. The actual orientation of the easy axis with respect to the current channel in these devices ( $\varphi_{\text{EA}}$ ) is further determined by angle-dependent anisotropic magnetoresistance (AMR) measurements (details of the determination of  $|\varphi_{\text{EA}}|$  can be found in Supplemental Material S2 [39]). Through the detection of the spin Hall effective-field-modified AMR or unidirectional magnetoresistance [14,43,44], current-induced magnetization switching can be observed in these samples under zero-field conditions. When the SOT-induced switching occurs,  $\Delta R_{\text{xx}}$  can be detected [14]. As shown in Fig. 4(b), the switching current,  $I_c$ , measured with  $t_{\text{pulse}} = 50$  ms decreases from 6.0 to 2.3 mA with increasing  $\varphi_{\text{EA}}$ .

We further perform pulse-width-dependent SOT switching measurements. As shown in Fig. 4(c), the SOT-induced magnetization switching for such a long pulse width ( $50 \text{ ms} \leq t_{\text{pulse}} \leq 1 \text{ s}$ ) is a thermally activated process, and the critical switching current,  $I_c$ , becomes larger as  $t_{\text{pulse}}$  decreases. The zero-thermal-fluctuation critical switching

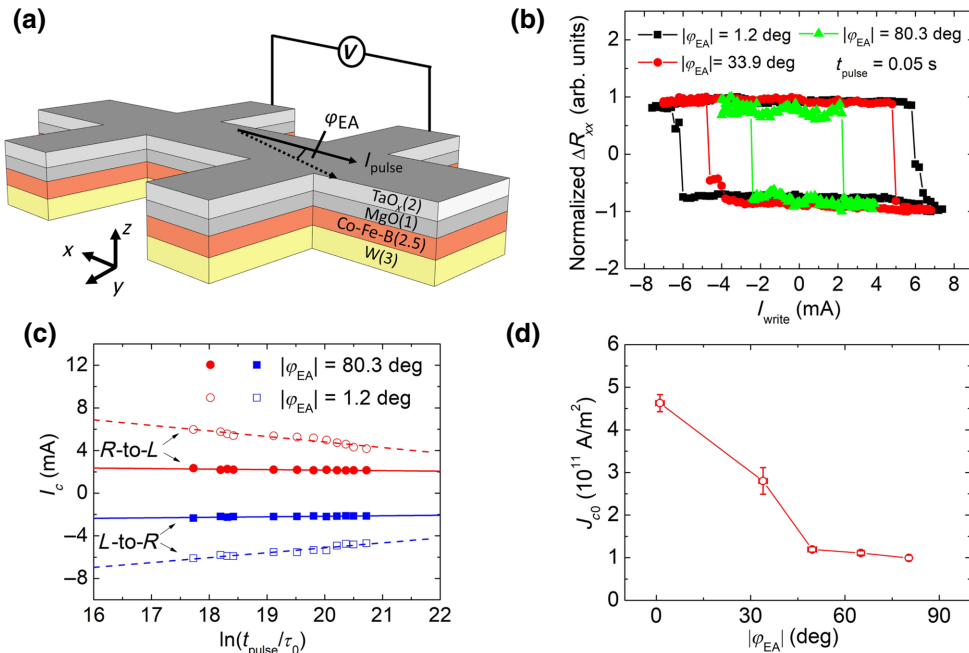


FIG. 4. Experiments. (a) Schematic illustration of a W(3)/Co-Fe-B(2.5)/MgO(1) Hall-bar device and current-induced magnetization switching measurement. Direction of positive current is defined the along  $-x$  direction. (b) Representative  $\Delta R_{\text{xx}}$  as a function of write current,  $I_{\text{write}}$ , for W(3)/Co-Fe-B(2.5)/MgO(1) devices with different  $\varphi_{\text{EA}}$ . (c) Write-current pulse-width dependence of the critical switching current,  $I_c$ , for W(3)/Co-Fe-B(2.5)/MgO(1) devices. (d) Zero-thermal-fluctuation critical switching-current density,  $J_{c0}$  as a function of the easy-axis canting angle,  $\varphi_{\text{EA}}$ .

current,  $I_{c0}$ , can be further obtained by [45]

$$I_c = I_{c0} \left[ 1 - \frac{1}{\Delta} \ln \left( \frac{t_{\text{pulse}}}{\tau_a} \right) \right], \quad (4)$$

where  $\Delta$  is the thermal stability factor and  $\tau_a \approx 1$  ns is the attempt timescale for thermally activated switching [46]. By using data in Fig. 4(c) and Eq. (4), we find that  $J_{c0} \approx 4.63 \times 10^{11}$  A/m<sup>2</sup> with  $\Delta \approx 64$  for the  $|\varphi_{\text{EA}}| = 1.2^\circ$  device and  $J_{c0} \approx 0.99 \times 10^{11}$  A/m<sup>2</sup> with  $\Delta \approx 30$  for the  $\varphi_{\text{EA}} = 80.3^\circ$  device.  $J_{c0}$  values for all annealed Hall-bar devices with different  $\varphi_{\text{EA}}$  are summarized in Fig. 4(d). The zero-thermal-fluctuation critical switching-current density sharply decreases from  $J_{c0} \approx 4.63 \times 10^{11}$  A/m<sup>2</sup> for  $|\varphi_{\text{EA}}| = 1.2^\circ$  to  $J_{c0} \approx 1.19 \times 10^{11}$  A/m<sup>2</sup> for  $|\varphi_{\text{EA}}| = 33.9^\circ$  and is almost saturated at  $J_{c0} \approx 1.00 \times 10^{11}$  A/m<sup>2</sup> for  $|\varphi_{\text{EA}}| = 80.3^\circ$ . The trend of  $J_{c0}$  versus  $|\varphi_{\text{EA}}|$  from the experiments is qualitatively consistent with that from the simulations, which suggests that the canting-angle effect on switching-current density exists, even in microsized devices. The experimental results show a more gradual trend and a larger threshold canting angle compared with Fig. 3(d), which is attributed to the existence of the FLT in our samples. Notably, a similar trend between  $J_c$  and  $\varphi_{\text{EA}}$  is also observed in the in-plane magnetized elliptic nanodot array with various easy-axis directions through differential planar Hall effect measurements [31].

## F. Fieldlike torque contribution and the switching phase diagram

In most of the previous SOT switching studies, DLT has been regarded as the primary driving mechanism. Recent theoretical studies suggest the addition of FLT with an appropriate magnitude can assist magnetization switching and apparently reduce the switching current [47,48]. This sizeable FLT, which is a combined effect from the bulk SHE, interfacial REE, and Oersted field, is observed in various HM/FM heterostructures via spin-torque ferromagnetic resonance measurements and harmonic measurements [49–51]. It is therefore valid to say that the possible contribution of FLT to SOT switching cannot be entirely neglected.

To systematically investigate the effect of FLT in a type- $x$  system, we introduce an additional FLT term into Eq. (1), which is expressed as

$$\tau_{\text{FL}} = \gamma \frac{\hbar(\eta\xi_{\text{DL}})J}{2eM_s t_{\text{FM}}} (\hat{\sigma} \times \mathbf{m}), \quad (5)$$

where  $\eta$  is a dimensionless FLT-to-DLT ratio ( $\equiv \xi_{\text{FL}}/\xi_{\text{DL}}$ ). In this section, the pillar orientation of the type- $x$  structure is canted by  $1^\circ$  to achieve field-free switching. The applied current density is swept from 0.0 to  $11.0 \times 10^{12}$  A/m<sup>2</sup> with 5-ns duration, and we record the  $x$  component of

magnetization after 5-ns relaxation. By varying the FLT-to-DLT ratio from +1 to -1 (corresponding to  $\xi_{\text{FL}} = -0.5$  to +0.5), we arrive at the phase diagram shown in Fig. 5(a), in which the white (red) region in the phase diagram represents the magnetization being switched (not being switched). This phase diagram can be divided into four regions, namely, nonswitching, random switching, toggle switching, and deterministic switching regions.

For the part where the FLT-to-DLT ratio is  $>0$  in the switching phase diagram [Fig. 5(a)], it contains a deterministic switching region (white) and a nonswitching region (red). The deterministic switching region expands with increasing FLT-to-DLT ratio because FLT of the same sign can accelerate energy dissipation and facilitate magnetization stabilization. In this region, a larger FLT can significantly reduce the critical switching-current density.

To gain a further insight into the switching dynamics for a FLT-to-DLT ratio of  $<0$ , we extract magnetization trajectories in the nonswitching region, random switching region, toggle switching region, and deterministic switching region in the phase diagram for a FLT-to-DLT ratio of -0.4. When the applied current density is large enough, deterministic switching can be observed. As shown in Fig. 5(b), the magnetization is aligned along  $+y$  but with a slight deviation (towards the  $x$  direction) from it due to the small canting angle. After relaxation, magnetization can be successfully switched. In the deterministic switching region, DLT is the dominating term to drive magnetization switching.

As the current density is lowered down to about  $8.42 \times 10^{12}$  A/m<sup>2</sup>, toggle switching will occur. As shown in Fig. 5(c), magnetization will stop at a position with a large  $+z$  component before relaxation. For lower current densities, magnetization before relaxation will stabilize at a position with a higher  $+z$  component and smaller  $+y$  and  $+x$  components. The magnitude of  $m_z$  after excitation of the SOT will affect the final orientation of magnetization (switched or not switched) after relaxation, since different  $m_z$  values will lead to different precession cycle numbers. We can define the precession number,  $N$ , as the number of times magnetization passes the  $y$ - $z$  plane during the relaxation process. In this region, a smaller applied current density corresponds to larger  $m_z$  and a larger  $N$ . As the current density decreases, the behavior of  $N$  becomes a staircase function. If  $N$  is an odd (even) number, we define the normalized  $N$ ,  $N_{\text{nor}}$ , as  $+1$  ( $-1$ ). As shown in Fig. 5(d), depending on  $N$ , magnetization switches after half cycles of precession ( $N_{\text{nor}} = -1$ ) and does not switch after full cycles of precession ( $N_{\text{nor}} = +1$ ). This result is also consistent with an earlier macrospin study that considered a nonzero FLT-to-DLT ratio in the type- $z$  system [48].

For the random switching region, there are two types of magnetization dynamics during excitation of the SOT, namely, precession and oscillation. The magnetization trajectories of precession and oscillation dynamics are shown

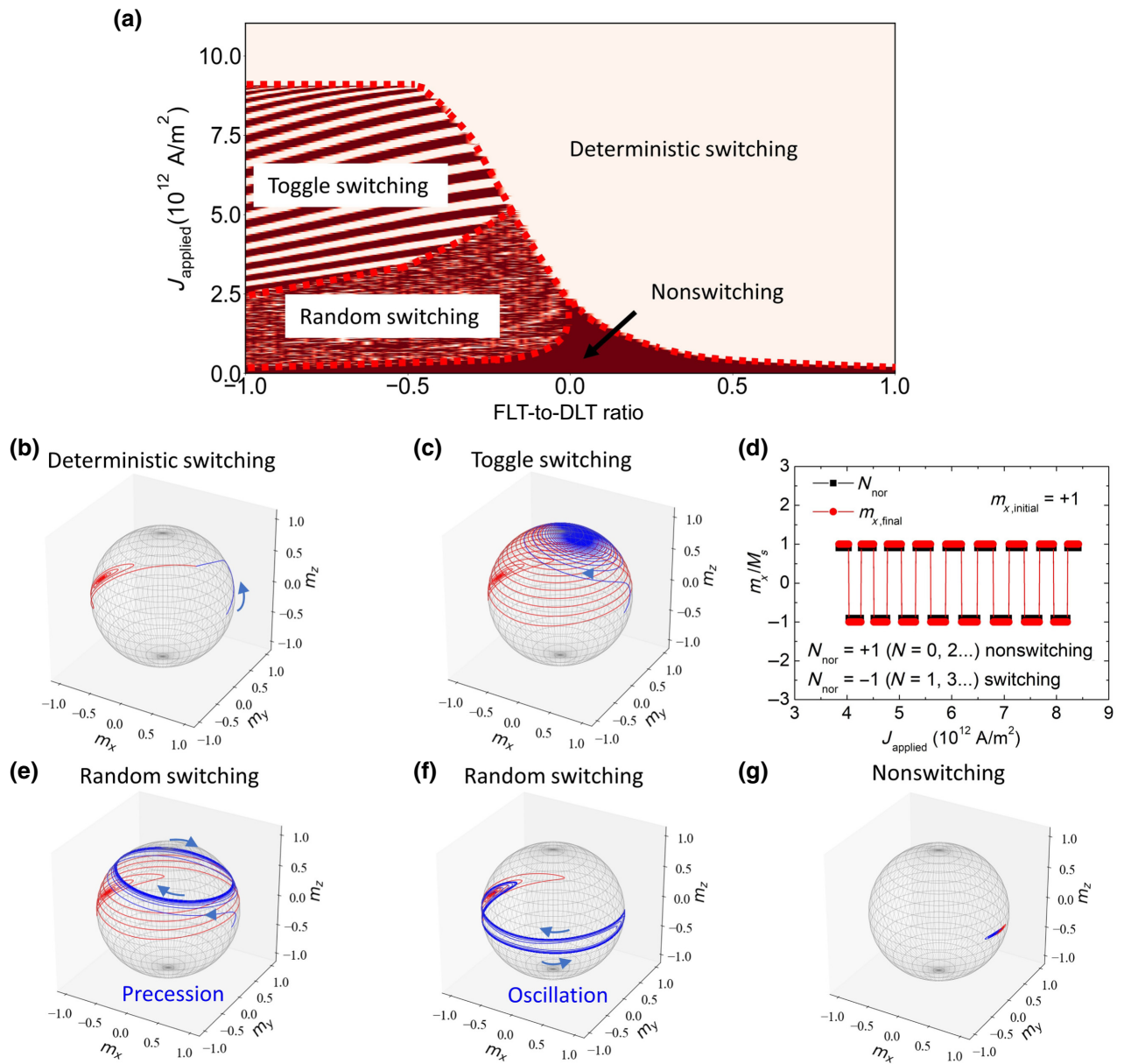


FIG. 5. Macrospin simulations. (a) Switching phase diagram of a type- $x$  device ( $\varphi = 1^\circ$ ) at various FLT-to-DLT ratios with a fixed DLT efficiency of 0.5. Magnetization trajectories for FLT/DLT =  $-0.4$  in (b) deterministic switching region with  $J_{\text{applied}} = 9.56 \times 10^{12} \text{ A/m}^2$ , (c) toggle switching region with  $J_{\text{applied}} = 4.19 \times 10^{12} \text{ A/m}^2$ , (e) precession dynamics before relaxation in the random switching region with  $J_{\text{applied}} = 2.21 \times 10^{12} \text{ A/m}^2$ , (f) oscillation dynamics before relaxation in the random switching region with  $J_{\text{applied}} = 0.37 \times 10^{12} \text{ A/m}^2$ , and (g) nonswitching region with  $J_{\text{applied}} = 0.15 \times 10^{12} \text{ A/m}^2$ . (d) Normalized precession number,  $N_{\text{nor}}$ , and  $m_x$  as functions of  $J_{\text{applied}}$  in the toggle switching region with FLT/DLT =  $-0.4$ .

in Figs. 5(e) and 5(f), respectively. This kind of steady tilted precession is caused by the dynamic equilibrium between the FLT, DLT, and demagnetization field torque with a larger applied current density. The final state of magnetization also depends on the precession number,  $N$ , during 5-ns relaxation. For a lower applied current density in the random switching region, the oscillation dynamics emerges due to competition between the demagnetization field torque and the SOT. The sign of the  $x$  component of

the final magnetization position before relaxation decides whether magnetization is switched or not. If magnetization has a  $-x$  component before relaxation, magnetization will precess and stop at an almost  $-x$  direction, which means that magnetization switching is achieved. The existence of precession and oscillation modes has also been reported in a previous study [52], which points out that the magnitude of the FLT-to-DLT ratio can be modified by tuning the HM and FM layer thicknesses.



For the nonswitching region, a representative magnetization trajectory is shown in Fig. 5(g). The DLT is too small to overcome the energy barrier in the  $y$ - $z$  plane before relaxation; therefore, magnetization will stabilize in the initial position after relaxation. In short, FLT plays a crucial role in type- $x$  SOT-driven magnetization switching. For a FLT-to-DLT ratio of  $>0$ , the FLT can assist magnetization switching and reduce the critical switching-current density robustly. For a FLT-to-DLT ratio of  $<0$ , precession dominates the magnetization dynamics, thereby suppressing magnetization switching. This feature might be disadvantageous for memory applications but could be useful in probabilistic computing-related applications [53–55]. In the following section, we will focus on the potential of adopting type- $x$  SOT switching with a FLT-to-DLT ratio of  $>0$ .

### G. Fieldlike torque-assisted type- $x$ switching

Next, we study the variation of switching-current density with respect to the external field,  $\mu_0 H_z$ , and the canting angle,  $\varphi$ , with the inclusion of different FLT-to-DLT ratios.  $J_{sw}$  versus  $\mu_0 H_z$  curves with various FLT-to-DLT ratios

are shown in Fig. 6(a) ( $\varphi = 0^\circ$ ). As the FLT-to-DLT ratio increases, the slope of  $J_{sw}$  versus  $\mu_0 H_z$  decreases significantly due to enhancement of the FLT effective field. However, the  $x$  intercept remains constant ( $\mu_0 H_{z,0} = 0.40$  T) for each FLT-to-DLT ratio. The canting-angle dependences of  $J_{sw}$  at various FLT-to-DLT ratios are shown in Fig. 6(b), where the overall  $J_{sw}$  becomes lower with increasing FLT. The type- $x$  regime also expands to be much closer to  $90^\circ$  due to faster energy dissipation during precession, as assisted by the positive FLT.

To further investigate variations between type- $x$  ( $\varphi = 1^\circ$ ) and type- $y$  ( $\varphi = 90^\circ$ ) systems in the short current-pulse-width regime, we calculate the switching current,  $I_{sw}$ , for these two types of systems with  $0.1 \text{ ns} \leq t_{pulse} \leq 10 \text{ ns}$  and 5-ns relaxation at various FLT-to-DLT ratios. The current-channel width and shape of the pillar are set to be the same as those in Fig. 4(c) for type  $x$  ( $\varphi = 1^\circ$ ) and type  $y$  ( $\varphi = 90^\circ$ ). The  $I_{sw}$  versus  $t_{pulse}$  curve for a FLT-to-DLT ratio of 0.4 is shown in Fig. 6(c). Notice that the crossover point ( $t_{CO}$ ) between type- $x$  and type- $y$  systems migrates from 0.23 ns for a FLT-to-DLT ratio of 0.0 to 2.66 ns for a FLT-to-DLT ratio of 0.4.  $t_{CO}$  values for each FLT-to-DLT ratio are summarized in Fig. 6(d), in which

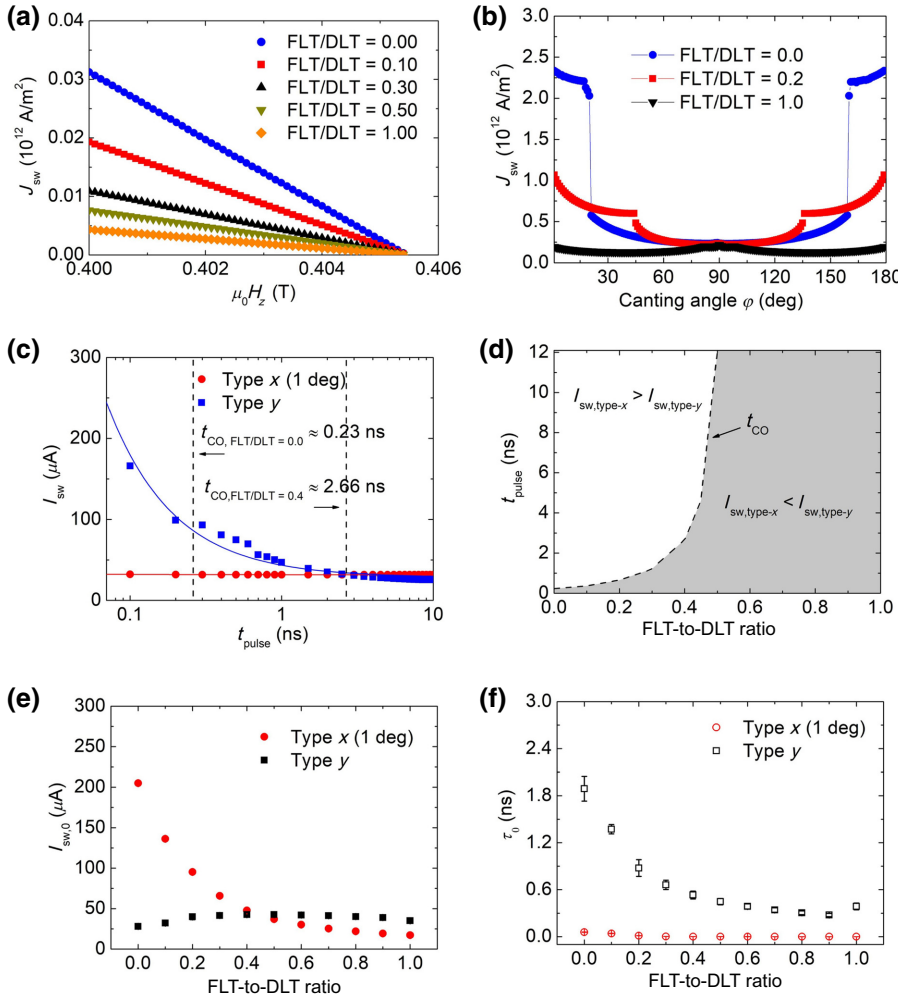


FIG. 6. Macrospin simulations. (a)  $J_{sw}$  vs  $\mu_0 H_z$  for type- $x$  structures with various FLT-to-DLT ratios. (b)  $J_{sw}$  vs canting angle ( $\varphi = 1^\circ$  to  $179^\circ$ ) with various FLT-to-DLT ratios. (c)  $t_{pulse}$  dependence of  $J_{sw}$  for type- $x$  ( $\varphi = 1^\circ$ ) and type- $y$  ( $\varphi = 90^\circ$ ) structures with FLT/DLT = 0.4. Dashed lines in (c) represent the crossover point,  $t_{CO}$ , between the type- $x$  and type- $y$  geometries. (d)  $I_{sw}$  phase diagram for type- $x$  ( $\varphi = 1^\circ$ ) and type- $y$  ( $\varphi = 90^\circ$ ) structures. Black dashed line in (d) represents  $t_{CO}$  between the type- $x$  and type- $y$  geometries with various positive FLT-to-DLT ratios. (e)  $I_{sw,0}$  and (f)  $\tau_0$  for type- $x$  ( $\varphi = 1^\circ$ ) and type- $y$  ( $\varphi = 90^\circ$ ) structures extracted with Eq. (3) as functions of the FLT-to-DLT ratio.

the gray region represents  $I_{sw}$  of type  $y$  being larger than that of type  $x$  (more advantageous to adopt type  $x$ ).

Again, the intrinsic critical switching current,  $I_{sw,0}$ , and precession time,  $\tau_0$ , can be obtained from  $I_{sw,0}$  versus  $t_{pulse}$  curves for each FLT-to-DLT ratio from Eq. (3). Figures 6(e) and 6(f) show  $I_{sw,0}$  and  $\tau_0$  versus FLT-to-DLT ratio.  $I_{sw,0}$  of type- $x$  structure decreases with increasing FLT-to-DLT ratio and becomes smaller than that of type  $y$  at a FLT-to-DLT ratio of 0.5. For type  $y$ , the precession time,  $\tau_0$ , decreases from 1.8 to 0.3 ns with increasing FLT-to-DLT ratio from 0.0 to 1.0. For type  $x$ ,  $\tau_0$  also drops from 50 to 0.4 ps as the FLT-to-DLT ratio increases. However, type  $x$  has a much smaller  $\tau_0$  for the whole range of FLT-to-DLT ratios, which is indicative of the potential for much faster switching with the type- $x$  structure. Overall, we show that the performance of type  $x$  (lower  $I_{sw}$  and lower  $\tau_0$ ) can be better than that of the type- $y$  system with an appropriate FLT in the short-pulse regime.

Notably, to achieve a sizable FLT-to-DLT ratio, there are several possible feasible ways. One approach is to select a suitable spin Hall metal that intrinsically possesses a large positive FLT-to-DLT ratio, such as Ta [56,57] or Hf [58]. Second, interfacial engineering is a method to increase the positive FLT-to-DLT ratio as well. It is shown that the ratio is enhanced via the insertion of a light metal layer between the spin Hall metal and the FM layer [59]. Moreover, the annealing temperature can also be optimized to obtain a large FLT-to-DLT ratio [60].

## H. Micromagnetic simulations

To mimic magnetic dynamics in real devices with the type- $x$  structure, we further perform micromagnetic

simulations with Mumax3 [61]. Additional material parameters included in micromagnetic simulations are summarized in Table II. The exchange-stiffness constant is set as  $1.6 \times 10^{-11}$  J/m, and the strength of the interfacial Dzyaloshinskii-Moriya interaction (DMI) is  $2 \times 10^{-4}$  J/m<sup>2</sup>, which are both referenced to typical values for Co-Fe-B [62]. The macrospin simulations show that  $K_u$  does not prominently influence  $J_{sw}$ . It remains of the same order, even when  $K_u$  is added up to  $10^5$  J/m<sup>3</sup> with the same  $\mu_0 H_z$  applied. Consequently, we tentatively set  $K_u$  as zero to conduct micromagnetic simulations for simplicity.

Similar to the macrospin results, Fig. 7(a) shows that  $J_{sw}$  decreases linearly as  $\mu_0 H_z$  increases until it reaches zero at around  $\mu_0 H_z = 0.39$  T. The slope fitted is  $-5.8 \times 10^{12}$  A/Tm<sup>2</sup>, which is also in line with the macrospin results [Fig. 2(a)]. Figure 7(b) shows  $J_{sw}$  as a function of  $\varphi$  from 3° to 177° for various FLT-to-DLT ratios. For small FLT-to-DLT ratios (0 and 0.2), the transitions from type- $x$ -like to type- $y$ -like behavior appear at  $\varphi \sim 27^\circ$  and  $153^\circ$ , which are slightly different from the results of macrospin simulations. This slight discrepancy is tentatively attributed to the inclusion of the DMI and exchange interactions in micromagnetic simulations. In either the type- $x$  or type- $y$  regime,  $J_{sw}$  is smaller as the canting angle approaches 90° (i.e.,  $J_{sw}$  decreases as the system looks more analogous to type  $y$ ), meaning that type  $x$  is not as efficient as type  $y$  with a small FLT. However,  $J_{sw}$  drops significantly, and the type- $x$  regime broadens as the FLT-to-DLT ratio becomes larger. When the FLT-to-DLT ratio is one, the boundary between the type- $x$  and type- $y$  regime becomes ambiguous. Again, we observe that type  $x$  is inferior to type  $y$  when FLT is small or absent but

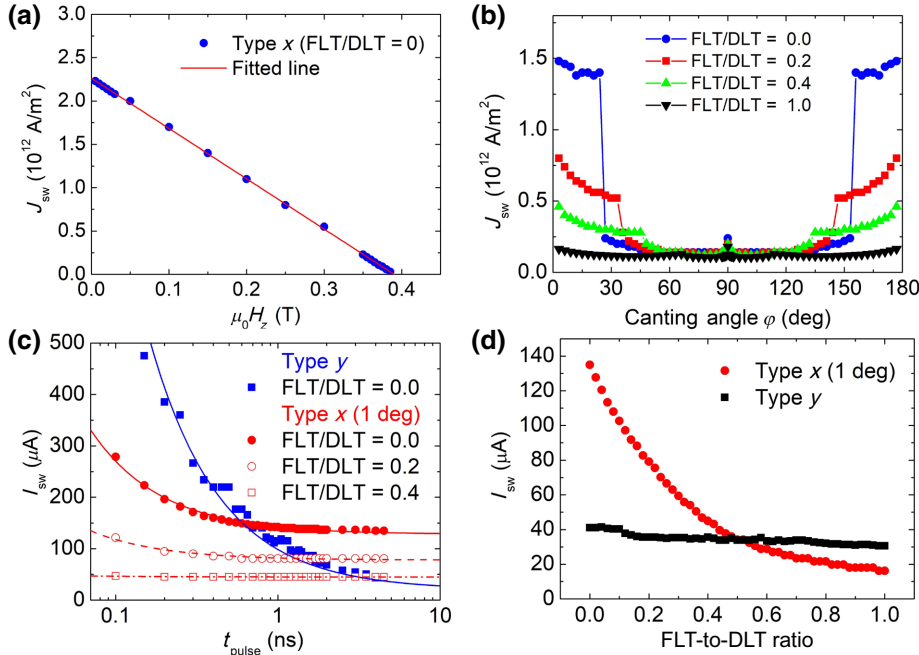


FIG. 7. Micromagnetic simulations. (a)  $\mu_0 H_z$  dependence of  $J_{sw}$  for type- $x$  structure obtained by micromagnetic simulations. (b) Canting-angle dependence of  $J_{sw}$  with various FLT-to-DLT ratios. (c) Pulse-width dependence of  $I_{sw}$  with various FLT-to-DLT ratios, and (d) FLT-to-DLT ratio dependence of  $I_{sw}$  for type- $x$  ( $\varphi = 1^\circ$ ) and type- $y$  ( $\varphi = 90^\circ$ ) structures. Notably, in (c), type- $y$  curve is simulated without FLT and other type- $x$  curves are simulated with  $\varphi = 1^\circ$ .

TABLE III. Fitted parameters ( $I_{sw,0}$  and  $\tau_0$ ) of type- $y$  and type- $x$  switching with different FLT-to-DLT ratios, according to Eq. (3).  $t_{CO}$  is the crossover point of the type- $x$  curve with respect to the type- $y$  curve.

	$I_{sw,0}(\mu A)$	$\tau_0$ (ns)	$t_{CO}$ (ns)
Type $y$ ( $\varphi = 90^\circ$ ) FLT/DLT = 0.0	19.71	4.00	NA
Type $x$ ( $\varphi = 1^\circ$ ) FLT/DLT = 0.0	128.16	0.11	0.60
Type $x$ ( $\varphi = 1^\circ$ ) FLT/DLT = 0.2	77.90	0.051	1.29
Type $x$ ( $\varphi = 1^\circ$ ) FLT/DLT = 0.4	44.85	0.0033	3.13

may become advantageous over type  $y$  when the FLT is large enough.

Next, we look into the performance of type- $x$  ( $\varphi = 1^\circ$ ) and type- $y$  ( $\varphi = 90^\circ$ ) structures when short current pulses ( $t_{pulse} \leq 5$  ns) are applied. Figure 7(c) shows the critical switching current,  $I_{sw}$ , as a function of current pulse width,  $t_{pulse}$ , for various positive FLT-to-DLT ratios. Notably, the relaxation time is 5 ns and the width of the current channel considered here is the same as that shown in Fig. 3(c). Data points are all fitted with Eq. (3). The extracted  $I_{sw,0}$  and  $\tau_0$  from each curve and  $t_{CO}$  are summarized in Table III. For current pulses shorter than  $t_{CO}$ , type  $x$  ( $\varphi = 1^\circ$ ) has a smaller  $I_{sw}$  than type  $y$ , indicating that type  $x$  performs better within this regime. As the FLT-to-DLT ratio increases from 0 to 0.4,  $t_{CO}$  increases from 0.60 to 3.13 ns. The trend of  $t_{CO}$  versus FLT-to-DLT ratio again suggests that, from the perspective of designing type- $x$  SOT MRAM, a sizable FLT can be beneficial for the reduction of  $I_{sw}$  and enhancement of  $t_{CO}$ .

Finally, we simulate the FLT-to-DLT ratio dependence of  $I_{sw}$ . Notably, the pulse duration and relaxation time here are both fixed as 5 ns. Figure 7(d) shows  $I_{sw}$  as a function of positive FLT-to-DLT ratio for type- $x$  ( $\varphi = 1^\circ$ ) and type- $y$  structures. As shown in Fig. 7(d),  $I_{sw}$  of type  $y$  only decreases slightly with increasing FLT-to-DLT ratio, while that of type  $x$  is inversely proportional to the FLT-to-DLT ratio. The results show that, when the FLT-to-DLT ratio is larger than 0.5, type- $x$  has a smaller  $I_{sw}$  than type  $y$ , which is consistent with the results in Fig. 6(e) obtained by macrospin simulations. This trend again suggests that FLT indeed plays a critical role in promoting the application of type- $x$  devices.

### III. CONCLUSION

We scrutinize the features of a type- $x$  SOT switching scheme in nanosized HM/FM bilayer structures by numerical simulations. Through macrospin simulations, we demonstrate that the switching-current density,  $J_{sw}$ ,

depends on  $\mu_0 H_z$  and the shape-anisotropy field (including  $\mu_0 H_{k,in}$  and  $\mu_0 H_{k,out}$ ). We show that type  $x$  is only more efficient than type  $y$  when the applied pulse is shorter than a crossover timescale of  $t_{CO} \sim 0.23$  ns. The trend of  $\varphi$  versus  $J_{sw}$  obtained from simulations is consistent with experimental results. To explore the effects of FLT, we obtain a detailed switching phase diagram that provides an insight into the magnetization dynamics for applications using type- $x$  geometry. Moreover, through both macrospin and micromagnetic simulations, we show that a positive FLT-to-DLT ratio reduces the switching current,  $I_{sw}$ , considerably, and the window of ultrafast type- $x$  SOT switching can be expanded with increasing FLT. Therefore, by optimizing the geometry of the FM pillar and adopting materials with suitable FLT efficiency, type- $x$  geometry is anticipated to be a promising scheme for future SOT MRAM applications.

### ACKNOWLEDGMENTS

This work is supported by the Ministry of Science and Technology of Taiwan (MOST) under Grant No. MOST-110-2636-M-002-013 and by the Center of Atomic Initiative for New Materials (AI-Mat) and the Advanced Research Center of Green Materials Science and Technology, National Taiwan University, from the Featured Areas Research Center Program within the framework of the Higher Education Sprout Project by the Ministry of Education (MOE) in Taiwan under Grant No. NTU-110L9008. We also thank Shy-Jay Lin of the Taiwan Semiconductor Manufacturing Company for fruitful discussions.

- [1] A. Hoffmann, Spin Hall effects in metals, *IEEE Trans. Magn.* **49**, 5172 (2013).
- [2] J. Sinova, S. O. Valenzuela, J. Wunderlich, C. H. Back, and T. Jungwirth, Spin Hall effects, *Rev. Mod. Phys.* **87**, 1213 (2015).
- [3] I. M. Miron, K. Garello, G. Gaudin, P. J. Zermatten, M. V. Costache, S. Auffret, S. Bandiera, B. Rodmacq, A. Schuhl, and P. Gambardella, Perpendicular switching of a single ferromagnetic layer induced by in-plane current injection, *Nature* **476**, 189 (2011).
- [4] L. Liu, C. F. Pai, D. C. Ralph, and R. A. Buhrman, Magnetic Oscillations Driven by the Spin Hall Effect in 3-Terminal Magnetic Tunnel Junction Devices, *Phys. Rev. Lett.* **109**, 186602 (2012).
- [5] V. E. Demidov, S. Urazhdin, H. Ulrichs, V. Tiberkevich, A. Slavin, D. Baither, G. Schmitz, and S. O. Demokritov, Magnetic nano-oscillator driven by pure spin current, *Nat. Mater.* **11**, 1028 (2012).
- [6] R. H. Liu, W. L. Lim, and S. Urazhdin, Spectral Characteristics of the Microwave Emission by the Spin Hall Nano-Oscillator, *Phys. Rev. Lett.* **110**, 147601 (2013).

- [7] S. Emori, U. Bauer, S. M. Ahn, E. Martinez, and G. S. Beach, Current-driven dynamics of chiral ferromagnetic domain walls, *Nat. Mater.* **12**, 611 (2013).
- [8] P. P. Haazen, E. Mure, J. H. Franken, R. Lavrijsen, H. J. Swagten, and B. Koopmans, Domain wall depinning governed by the spin Hall effect, *Nat. Mater.* **12**, 299 (2013).
- [9] C.-F. Pai, M. Mann, A. J. Tan, and G. S. D. Beach, Determination of spin torque efficiencies in heterostructures with perpendicular magnetic anisotropy, *Phys. Rev. B* **93**, 144409 (2016).
- [10] L. Liu, C.-F. Pai, Y. Li, H. W. Tseng, D. C. Ralph, and R. A. Buhrman, Spin-torque switching with the giant spin Hall effect of tantalum, *Science* **336**, 555 (2012).
- [11] C.-F. Pai, L. Liu, Y. Li, H. W. Tseng, D. C. Ralph, and R. A. Buhrman, Spin transfer torque devices utilizing the giant spin Hall effect of tungsten, *Appl. Phys. Lett.* **101**, 122404 (2012).
- [12] T.-Y. Chen, H.-I. Chan, W.-B. Liao, and C.-F. Pai, Current-Induced Spin-Orbit Torque and Field-Free Switching in Mo-Based Magnetic Heterostructures, *Phys. Rev. Appl.* **10**, 044038 (2018).
- [13] T.-C. Wang, T.-Y. Chen, C.-T. Wu, H.-W. Yen, and C.-F. Pai, Comparative study on spin-orbit torque efficiencies from W/ferromagnetic and W/ferrimagnetic heterostructures, *Phys. Rev. Mater.* **2**, 014403 (2018).
- [14] Y.-T. Liu, T.-Y. Chen, T.-H. Lo, T.-Y. Tsai, S.-Y. Yang, Y.-J. Chang, J.-H. Wei, and C.-F. Pai, Determination of Spin-Orbit-Torque Efficiencies in Heterostructures with In-Plane Magnetic Anisotropy, *Phys. Rev. Appl.* **13**, 044032 (2020).
- [15] J. Z. Sun, Spin-current interaction with a monodomain magnetic body: A model study, *Phys. Rev. B* **62**, 570 (2000).
- [16] S. Fukami, T. Anekawa, C. Zhang, and H. Ohno, A spin-orbit torque switching scheme with collinear magnetic easy axis and current configuration, *Nat. Nanotechnol.* **11**, 621 (2016).
- [17] T. Taniguchi, Switching induced by spin Hall effect in an in-plane magnetized ferromagnet with the easy axis parallel to the current, *Phys. Rev. B* **102**, 104435 (2020).
- [18] Y. Shiokawa, E. Komura, Y. Ishitani, A. Tsumita, K. Suda, K. Hamanaka, T. Taniguchi, and T. Sasaki, Dependency of high-speed write properties on external magnetic field in spin-orbit torque in-plane magnetoresistance devices, *Appl. Phys. Express* **14**, 013001 (2021).
- [19] S. Fukami, T. Anekawa, A. Ohkawara, Z. Chaoliang, and H. Ohno, in IEEE Symposium on VLSI Technology, Vol. 61 (2016).
- [20] L. Liu, O. J. Lee, T. J. Gudmundsen, D. C. Ralph, and R. A. Buhrman, Current-Induced Switching of Perpendicularly Magnetized Magnetic Layers Using Spin Torque From the Spin Hall Effect, *Phys. Rev. Lett.* **109**, 096602 (2012).
- [21] Y. Fan, X. Kou, P. Upadhyaya, Q. Shao, L. Pan, M. Lang, X. Che, J. Tang, M. Montazeri, K. Murata, L. T. Chang, M. Akyol, G. Yu, T. Nie, K. L. Wong, J. Liu, Y. Wang, Y. Tserkovnyak, and K. L. Wang, Electric-field control of spin-orbit torque in a magnetically doped topological insulator, *Nat. Nanotechnol.* **11**, 352 (2016).
- [22] A. van den Brink, G. Vermijs, A. Solignac, J. Koo, J. T. Kohlhepp, H. J. M. Swagten, and B. Koopmans, Field-free magnetization reversal by spin-Hall effect and exchange bias, *Nat. Commun.* **7**, 10854 (2016).
- [23] T. C. Chuang, C. F. Pai, and S. Y. Huang, Cr-induced Perpendicular Magnetic Anisotropy and Field-Free Spin-Orbit-Torque Switching, *Phys. Rev. Appl.* **11** (2019).
- [24] S. C. Baek, V. P. Amin, Y. W. Oh, G. Go, S. J. Lee, G. H. Lee, K. J. Kim, M. D. Stiles, B. G. Park, and K. J. Lee, Spin currents and spin-orbit torques in ferromagnetic trilayers, *Nat. Mater.* **17**, 509 (2018).
- [25] Y. Sheng, K. W. Edmonds, X. Ma, H. Zheng, and K. Wang, Adjustable current-induced magnetization switching utilizing interlayer exchange coupling, *Adv. Electron. Mater.* **4** (2018).
- [26] N. Murray, W.-B. Liao, T.-C. Wang, L.-J. Chang, L.-Z. Tsai, T.-Y. Tsai, S.-F. Lee, and C.-F. Pai, Field-free spin-orbit torque switching through domain wall motion, *Phys. Rev. B* **100**, 104441 (2019).
- [27] J. M. Lee, K. Cai, G. Yang, Y. Liu, R. Ramaswamy, P. He, and H. Yang, Field-free spin-orbit torque switching from geometrical domain-wall pinning, *Nano Lett.* **18**, 4669 (2018).
- [28] Q. Ma, Y. Li, D. B. Gopman, Y. P. Kabanov, R. D. Shull, and C. L. Chien, Switching a Perpendicular Ferromagnetic Layer by Competing Spin Currents, *Phys. Rev. Lett.* **120**, 117703 (2018).
- [29] Z. A. Bekele, X. Liu, Y. Cao, and K. Wang, High-efficiency spin-orbit torque switching using a single heavy-metal alloy with opposite spin Hall angles, *Adv. Electron. Mater.* **7** (2020).
- [30] Y. Cao, Y. Sheng, K. W. Edmonds, Y. Ji, H. Zheng, and K. Wang, Deterministic magnetization switching using lateral spin-orbit torque, *Adv. Mater.* **32**, e1907929 (2020).
- [31] Y. Takahashi, Y. Takeuchi, C. Zhang, B. Jinnai, S. Fukami, and H. Ohno, Spin-orbit torque-induced switching of in-plane magnetized elliptical nanodot arrays with various easy-axis directions measured by differential planar Hall resistance, *Appl. Phys. Lett.* **114**, 012410 (2019).
- [32] Q. Hao and G. Xiao, Giant Spin Hall Effect and Switching Induced by Spin-Transfer Torque in a W/Co<sub>40</sub>Fe<sub>40</sub>B<sub>20</sub>/MgO Structure with Perpendicular Magnetic Anisotropy, *Phys. Rev. Appl.* **3**, 034009 (2015).
- [33] S. Mondal, S. Choudhury, N. Jha, A. Ganguly, J. Sinha, and A. Barman, All-optical detection of the spin Hall angle in W/CoFeB/SiO<sub>2</sub> heterostructures with varying thickness of the tungsten layer, *Phys. Rev. B* **96**, 054414 (2017).
- [34] W. Chen, G. Xiao, Q. Zhang, and X. Zhang, Temperature study of the giant spin Hall effect in the bulk limit of  $\beta$ -W, *Phys. Rev. B* **98**, 134411 (2018).
- [35] R. Bansal, G. Nirala, A. Kumar, S. Chaudhary, and P. K. Muduli, Large spin Hall angle in  $\beta$ -W thin films grown on CoFeB without oxygen plasma, *Spin* **08**, 1850018 (2019).
- [36] Y. Takeuchi, C. Zhang, A. Okada, H. Sato, S. Fukami, and H. Ohno, Spin-orbit torques in high-resistivity-W/CoFeB/MgO, *Appl. Phys. Lett.* **112**, 192408 (2018).
- [37] K.-S. Lee, S.-W. Lee, B.-C. Min, and K.-J. Lee, Threshold current for switching of a perpendicular magnetic layer induced by spin Hall effect, *Appl. Phys. Lett.* **102**, 112410 (2013).

- [38] M. Beleggia, M. D. Graef, Y. T. Millev, D. A. Goode, and G. Rowlands, Demagnetization factors for elliptical cylinders, *J. Phys. D: Appl. Phys.* **38**, 3333 (2005).
- [39] See the Supplemental Material at <http://link.aps.org/supplemental/10.1103/PhysRevApplied.16.024021> for the shape effect in switching-current density and anisotropy field and details of determining the canting angle for annealed samples by angle-dependent AMR measurements.
- [40] D. Bedau, H. Liu, J. Z. Sun, J. A. Katine, E. E. Fullerton, S. Mangin, and A. D. Kent, Spin-transfer pulse switching: From the dynamic to the thermally activated regime, *Appl. Phys. Lett.* **97**, 262502 (2010).
- [41] H. Liu, D. Bedau, J. Z. Sun, S. Mangin, E. E. Fullerton, J. A. Katine, and A. D. Kent, Dynamics of spin torque switching in all-perpendicular spin valve nanopillars, *J. Magn. Magn. Mater.* **358-359**, 233 (2014).
- [42] A. D. Kent and D. C. Worledge, A new spin on magnetic memories, *Nat. Nanotechnol.* **10**, 187 (2015).
- [43] C. O. Avci, K. Garello, A. Ghosh, M. Gabureac, S. F. Alvarado, and P. Gambardella, Unidirectional spin Hall magnetoresistance in ferromagnet/normal metal bilayers, *Nat. Phys.* **11**, 570 (2015).
- [44] C. O. Avci, J. Mendil, G. S. D. Beach, and P. Gambardella, Origins of the Unidirectional Spin Hall Magnetoresistance in Metallic Bilayers, *Phys. Rev. Lett.* **121**, 087207 (2018).
- [45] R. H. Koch, J. A. Katine, and J. Z. Sun, Time-Resolved Reversal of Spin-Transfer Switching in a Nanomagnet, *Phys. Rev. Lett.* **92**, 088302 (2004).
- [46] A. V. Khvalkovskiy, D. Apalkov, S. Watts, R. Chepulskii, R. S. Beach, A. Ong, X. Tang, A. Driskill-Smith, W. H. Butler, P. B. Visscher, D. Lottis, E. Chen, V. Nikitin, and M. Krounbi, erratum: Basic principles of STT-MRAM cell operation in memory arrays, *J. Phys. D: Appl. Phys.* **46**, 139601 (2013).
- [47] J. Park, G. E. Rowlands, O. J. Lee, D. C. Ralph, and R. A. Buhrman, Macrospin modeling of sub-ns pulse switching of perpendicularly magnetized free layer via spin-orbit torques for cryogenic memory applications, *Appl. Phys. Lett.* **105**, 102404 (2014).
- [48] W. Legrand, R. Ramaswamy, R. Mishra, and H. Yang, Coherent Subnanosecond Switching of Perpendicular Magnetization by the Fieldlike Spin-Orbit Torque Without an External Magnetic Field, *Phys. Rev. Appl.* **3**, 064012 (2015).
- [49] T. Nan, S. Emori, C. T. Boone, X. Wang, T. M. Oxholm, J. G. Jones, B. M. Howe, G. J. Brown, and N. X. Sun, Comparison of spin-orbit torques and spin pumping across NiFe/Pt and NiFe/Cu/Pt interfaces, *Phys. Rev. B* **91**, 214416 (2015).
- [50] C.-F. Pai, Y. Ou, L. H. Vilela-Leão, D. C. Ralph, and R. A. Buhrman, Dependence of the efficiency of spin Hall torque on the transparency of Pt/ferromagnetic layer interfaces, *Phys. Rev. B* **92**, 064426 (2015).
- [51] Y. Ou, C.-F. Pai, S. Shi, D. C. Ralph, and R. A. Buhrman, Origin of fieldlike spin-orbit torques in heavy metal/ferromagnet/oxide thin film heterostructures, *Phys. Rev. B* **94**, 140414 (2016).
- [52] C. Kim, B. S. Chun, J. Yoon, D. Kim, Y. J. Kim, I. H. Cha, G. W. Kim, D. H. Kim, K.-W. Moon, Y. K. Kim, and C. Hwang, Spin-orbit torque driven magnetization switching and precession by manipulating thickness of CoFeB/W heterostructures, *Adv. Electron. Mater.* **6**, 1901004 (2020).
- [53] N. Locatelli, A. Mizrahi, A. Accioly, R. Matsumoto, A. Fukushima, H. Kubota, S. Yuasa, V. Cros, L. G. Pereira, D. Querlioz, J. V. Kim, and J. Grollier, Noise-enhanced Synchronization of Stochastic Magnetic Oscillators, *Phys. Rev. Appl.* **2**, 034009 (2014).
- [54] K. Y. Camsari, R. Faria, B. M. Sutton, and S. Datta, Stochastic p-Bits for Invertible Logic, *Phys. Rev. X* **7**, 031014 (2017).
- [55] K. Y. Camsari, B. M. Sutton, and S. Datta, p-bits for probabilistic spin logic, *Appl. Phys. Rev.* **6**, 011305 (2019).
- [56] J. Kim, J. Sinha, M. Hayashi, M. Yamanouchi, S. Fukami, T. Suzuki, S. Mitani, and H. Ohno, Layer thickness dependence of the current-induced effective field vector in Ta|CoFeB|MgO, *Nat. Mater.* **12**, 240 (2013).
- [57] X. Qiu, P. Deorani, K. Narayanapillai, K. S. Lee, K. J. Lee, H. W. Lee, and H. Yang, Angular and temperature dependence of current induced spin-orbit effective fields in Ta/CoFeB/MgO nanowires, *Sci. Rep.* **4**, 4491 (2014).
- [58] R. Ramaswamy, X. Qiu, T. Dutta, S. D. Pollard, and H. Yang, Hf thickness dependence of spin-orbit torques in Hf/CoFeB/MgO heterostructures, *Appl. Phys. Lett.* **108**, 202406 (2016).
- [59] H.-Y. Lee, S. Kim, J.-Y. Park, Y.-W. Oh, S.-Y. Park, W. Ham, Y. Kotani, T. Nakamura, M. Suzuki, T. Ono, K.-J. Lee, and B.-G. Park, Enhanced spin-orbit torque via interface engineering in Pt/CoFeB/MgO heterostructures, *APL Mater.* **7**, 031110 (2019).
- [60] Z. Wang, H. Cheng, K. Shi, Y. Liu, J. Qiao, D. Zhu, W. Cai, X. Zhang, S. Eimer, D. Zhu, J. Zhang, A. Fert, and W. Zhao, Modulation of field-like spin orbit torque in heavy metal/ferromagnet heterostructures, *Nanoscale* **12**, 15246 (2020).
- [61] A. Vansteenkiste, J. Leliaert, M. Dvornik, M. Helsen, F. Garcia-Sanchez, and B. Van Waeyenberge, The design and verification of MuMax3, *AIP Adv.* **4**, 107133 (2014).
- [62] E. Grimaldi, V. Krizakova, G. Sala, F. Yasin, S. Couet, G. Sankar Kar, K. Garello, and P. Gambardella, Single-shot dynamics of spin-orbit torque and spin transfer torque switching in three-terminal magnetic tunnel junctions, *Nat. Nanotechnol.* **15**, 111 (2020).